

Anomalous dispersion in a dipole flow geometry

P. Kurowski, I. Ippolito, and J. P. Hulin

*Laboratoire de Physique et Mécanique des Milieux Hétérogènes (URA-CNRS No. 857), ESPCI,
10 rue Vauquelin, 75231 Paris Cedex 05, France*

J. Koplik

*Benjamin Levich Institute and Department of Physics, City College of the City University of New York,
New York, New York 10031*

E. J. Hinch

*Department of Applied Mathematics and Theoretical Physics, University of Cambridge, Silver Street,
Cambridge CB3 9EW, England*

(Received 30 March 1993; accepted 1 September 1993)

The dispersion of a passive tracer in fluid flowing between a source and a sink in a Hele–Shaw geometry, characteristic of field scale flows in a layer or fracture, is considered. A combination of analytic and numerical techniques and complementary experimental measurements are employed, leading to a consistent picture. This dispersion process is found to be characterized by a power-law decay in time of the tracer concentration, with an exponential cutoff at very long times, in strong contrast to the Gaussian behavior associated with the widely used quasi-one-dimensional (1-D) models.

I. INTRODUCTION

Many practical processes in groundwater hydrology and oil recovery involve the circulation of a fluid in a dipole geometry between an injection and a pumping well.^{1–4} For example, in geothermal operations one often wishes to recover heat by flowing water through an artificial or natural fracture network. Similarly, in secondary oil recovery one pumps water into injection wells in order to push oil toward the producing wells. In some cases, the number of wells is large and injection and pumping wells are located in alternate positions, so that the flow domain corresponding to each well is of limited size. At the other extreme, where only a single injection and a single pumping well are present, the flow lines may extend quite far from the two wells into zones of very low velocity. In this case, the transit times for the corresponding flow lines may be very large, so that the efficiency of the displacement process is reduced. The global extension of the fracture or of the porous layer into which fluid is injected will then be very important.

The purpose of the present paper is to study such effects in the simple model case of a circular fracture geometry, corresponding to the space between two parallel smooth planes. We have used a mixture of analytical, numerical, and experimental techniques to address the problem. The dipole flow is induced by a source and a sink placed symmetrically with respect to the fracture center, as indicated in Fig. 1. The fracture thickness is assumed to be small compared to its global radius. We have analyzed, in particular, the influence of the ratio between the source-sink separation a and the overall fracture radius R . We have chosen to analyze the dispersion of a passive tracer in this flow,^{5,6} since it provides the transit time distribution of fluid particles flowing between the source and the sink. This flow structure models a near horizontal fracture, or a thin stratum of porous rock, through which fluid is cir-

culated between two vertical wells intersecting the fracture or layer.⁷

The common practice in quantifying dispersion measurements is in terms of a quasi-one-dimensional (1-D) model,^{8–10} where a uniform average flow from source to sink is assumed. In ideal cases, the efflux profile, the concentration of tracer leaving the system as a function of time, is thereby fitted to a Gaussian or error function characteristic of solutions of the 1-D convection–diffusion equation. Commonly the ideal profile is not seen, and more complicated heuristic models, such as that of Coats and Smith,⁸ provide a better parametrization of the data. Such models retain the 1-D approximation, and are meant to allow for heterogeneity and, in particular, the presence of slow or stagnant fluid regions. Higher-dimensional modeling is generally avoided, except for purely radial flow or purely numerical studies, because of the paucity of analytic solutions of the convection–diffusion equation in two (2D) or three dimensions (3D).¹¹ The principal point of this paper is that dipolar flows are *qualitatively* different from 1-D models: Even if the medium is completely homogeneous one should expect power-law profiles cut off only by the effects of finite system volume. The distinction between one and higher dimensions can be seen most readily by considering the general theorem^{12,13} that the mean transit time for passive tracer convected through any system is given by the system volume divided by the flux. In a 1-D configuration containing a source and a sink, the volume is finite, given by the distance between the two. In the dipolar configurations considered here, or in any 3-D reservoir, the system volume is quite independent of the source-sink separation. Thus the mean transit time has no connection with a 1-D model and, as we shall see, the shape of the profile is quite different.

Several earlier papers in the hydrology literature have considered flow and dispersion in a dipole geometry, but with a different focus than ours. Hoopes and Harleman¹⁴

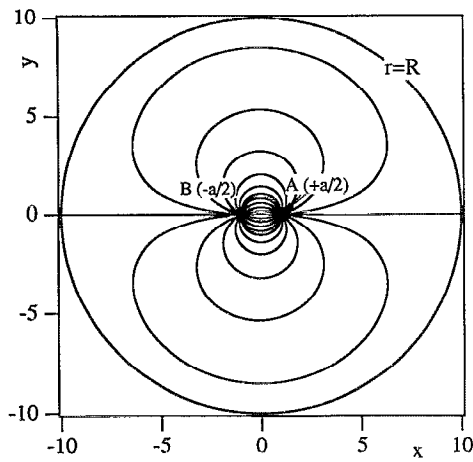


FIG. 1. Streamlines of the 2-D dipole velocity field induced by a source-sink flow. The source A and sink B are separated by 2 units and placed symmetrically about the center of a circle of radius 10 units bounding the fluid volume.

considered an infinite layer and found the tracer concentration profile in closed form in several limiting cases involving approximations to longitudinal dispersion, while Grove and Beeten¹⁵ solved for the tracer profile in a “crescent approximation,” which amounts to neglecting transverse dispersion. Aside from the approximations made, the effects of finite system size or the behavior at long times was not considered. In addition, numerical solution methods have been published by Huyakorn *et al.*¹⁶ and Gringarten, Sauty, and collaborators.¹⁷ Here the emphasis was on producing a curve of efflux tracer concentration versus time, with no attempt to extract the functional form of the result or to understand the nature of the transition between finite and infinite systems.

In Sec. II, we compute analytically the purely convective transit time distribution for a 2-D flow field, in the limiting case where the source-sink separation a tends to zero and the fracture radius R tends to infinity. We shall show that the concentration profile at the sink varies as a power law in time, due to the fact that the transit time increases as the cube of the maximum distance from the dipole along a trajectory. We shall then consider the influence of an outer boundary at finite radius, which is shown to introduce an exponential cutoff in the concentration variation at long times. Numerical computations of the concentration variation in the case of a finite R/a will then be performed to complement these results; they confirm the existence of a long-time exponential decay and show in addition that, while a power law variation regime is very often observed, the corresponding exponent may depend on the ratio R/a . The results of these 2-D computations will be finally compared to those of experimental measurements in Sec. III, where partial agreement is found. In Sec. IV we provide a more realistic theoretical treatment, by means of Monte-Carlo simulations, which takes into account both molecular diffusion and the parabolic flow profile between the parallel plates. Concluding remarks and indications for future work are given in Sec. V.

II. CONVECTIVE DISPERSION IN A 2-D DIPOLE GEOMETRY

In this section (only) we assume that the local flow velocity is independent of the vertical coordinate between the parallel plates, and we neglect molecular diffusion. In consequence, Taylor dispersion¹⁸ associated with the parabolic Poiseuille velocity profile in the fluid is omitted, although it will be restored later.

A. Perfect dipole in an infinite 2-D medium ($a \rightarrow 0$, $R \rightarrow \infty$)

Let us consider a source and a sink placed at $x = a/2$ and $-a/2$, respectively, in an infinite medium. The complex potential for the resultant flow is given by

$$W(z) = \frac{Q}{2\pi d} \left[\ln \left(z - \frac{a}{2} \right) - \ln \left(z + \frac{a}{2} \right) \right], \quad (1)$$

where $z = x + iy$, Q is the injected volumetric flow rate, and d is the fracture or layer thickness. In the case of a perfect dipole, where the distance a between the source and the sink tends to zero with constant moment $M = Qa$, $W(z)$ becomes

$$W(z) = -\frac{M}{2\pi d} \frac{1}{z} = -\frac{M}{2\pi d r} (\cos \theta - i \sin \theta) = \phi + i\psi, \quad (2)$$

where $z = r e^{i\theta}$, and ϕ and ψ are the velocity potential and streamfunction, respectively. The equation of the streamlines, on which ψ is a constant, takes the form

$$r = 2B \sin \theta, \quad (3)$$

corresponding to circles of radius B centered at the point $\{x=0, y=B\}$. Since the flow is stationary and diffusion is neglected, the streamlines are identical to the paths of the tracer particles.

From (2) we obtain the velocity field $\mathbf{v} = \text{grad } \phi$ and so the equation for the motion of the tracers is

$$\frac{dr}{dt} = v_r = \frac{M \cos \theta}{2\pi d r^2} \quad (4a)$$

and

$$r \frac{d\theta}{dt} = v_\theta = \frac{M \sin \theta}{2\pi d r^2} \quad (4b)$$

in polar coordinates, whence

$$dt = \frac{r d\theta}{v_\theta} = \frac{2\pi d r^3(\theta)}{M \sin \theta} d\theta.$$

By combining the above relation with Eq. (3) and integrating from $\theta=0$, we obtain

$$t_B(\theta) = \frac{8\pi d B^3}{M} \left(\theta - \frac{1}{2} \sin 2\theta \right). \quad (5)$$

Here, $t_B(\theta)$ is the time taken by the radius vector linking the origin to a tracer particle to turn through an angle θ as the particle moves along a circle of radius B , so that $t_B(\pi) = (8\pi^2 d/M) B^3$ is the time at which the particle will return to the sink. Note that t_B increases as the cube of the

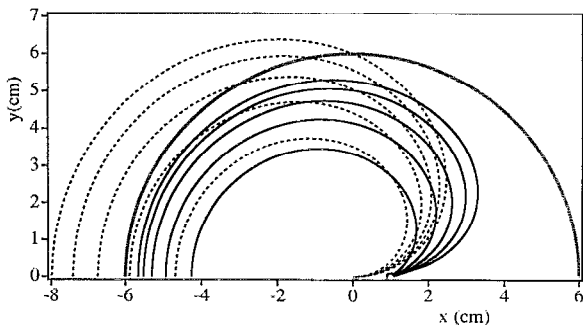


FIG. 2. Contours of the zones invaded at equally spaced times by dipole flows. Dipole with a finite source-sink distance $a=2$ cm in a model of radius $R=6$ cm (continuous lines). The thick shaded circle represents the boundary of the model. The dipole strength Qa and the injection times are such that the ratio V_{inj}/V_c of the injected volume and of the model volume has the values: 0.95, 1.9, 2.86, 3.63, 4.76. The curves on the inside correspond to the shortest times. In this particular example, the source is located at the left and the sink on the right. Perfect dipole in an infinite space (thin dotted line). The dipole strength Qa and the injection time values are the same as for the finite model.

radius B of the trajectory; indeed, t_B is of the order of the quotient of the path length ($\propto B$) and the particle velocity [which, from Eq. (4) varies as $1/B^2$]. The fast decrease of velocity with distance is demonstrated in Fig. 1, where flow lines corresponding to near direct trajectories are much more closely spaced than those extending far from the dipole.

Eliminating B using relation (3) and using $M=Qa$, we obtain the equation of the boundary of the injected solution at a given time t :

$$r(\theta) = \left(\frac{Qat}{\pi d} \right)^{1/3} \frac{\sin \theta}{(\theta - \sin 2\theta/2)^{1/3}}. \quad (6)$$

The dotted lines in Fig. 2 show the contours of the curves determined by Eq. (6) for different injected fluid volumes Qt : they enclose an area

$$S(t) = 2 \int_0^\pi d\theta \int_0^{r(\theta)} r dr.$$

The volume $V(t) = dS(t)$ occupied by the injected solution inside the cell can therefore be readily computed to be

$$V(t) = k_0 \left(\frac{a^2 d}{\pi^2} \right)^{1/3} (Qt)^{2/3}, \quad (7a)$$

where

$$k_0 = \int_0^\pi \frac{\sin^2 \theta}{(\theta - \sin^2 \theta/2)^{2/3}} d\theta \approx 2.1. \quad (7b)$$

Note that, from Eqs. (5) and (7), both $r(\theta)$ and $V(t)$ are independent of the flow rate Q for a given injected volume Qt . Note also that the volume $V(t)$ occupied by the fluid is much smaller than the injected volume Qt because most of the fluid short circuits from the source to the sink.

We now compute the normalized concentration of tracer in the fluid flowing out of the model:

$$\tilde{C}(t) = \frac{C_2 - C(t)}{C_2 - C_1}.$$

Here, C_2 is the tracer concentration in the injected fluid and C_1 the initial concentration so that $\tilde{C}(t)$ decreases from an initial unit value toward zero at long times. Also, $\tilde{C}(t)$ can be viewed as the relative fraction of displaced fluid in the solution flowing out of the fracture so that $Q\tilde{C}(t)dt$ is the amount of initial solution which gets displaced between times t and $t+dt$. Then,

$$V(t) = \int_0^t Q\tilde{C}(t)dt. \quad (8)$$

By comparing Eqs. (7) and (8), we obtain finally

$$\tilde{C}(t) = \frac{2}{3} k_0 \left(\frac{a^2 d}{\pi^2} \right)^{1/3} (Qt)^{-1/3}. \quad (9)$$

Therefore, the relative concentration varies with time following a power law, completely different from the error function dependence corresponding to the 1-D solutions of the advection-diffusion equation.

B. Long-time tracer dispersion characteristics for a finite-size model

Let us first assume that the source-sink distance is still infinitely small but the circular cell radius has a finite radius R . Then, using the method of images, the complex potential is

$$W(z) = -\frac{M}{2\pi d} \left(\frac{1}{z} + \frac{z}{R^2} \right). \quad (10)$$

This corresponds to the superimposition of the previous dipole flow and a uniform flow. Using Eqs. (4a) and (4b), the velocity field becomes

$$v_r = \frac{dr}{dt} = \frac{M \cos \theta}{2\pi d} \left(\frac{1}{r^2} - \frac{1}{R^2} \right), \quad (11a)$$

$$v_\theta = r \frac{d\theta}{dt} = \frac{M \sin \theta}{2\pi d} \left(\frac{1}{r^2} + \frac{1}{R^2} \right). \quad (11b)$$

The streamfunction Ψ associated with (10) is

$$\Psi(z) = \frac{M \sin \theta}{2\pi d} \left(\frac{1}{r} - \frac{r}{R^2} \right). \quad (11c)$$

At short times, the boundaries of the cell have a negligible influence on the transit time distribution of the tracer particles and $\tilde{C}(t)$ follows Eq. (9).

At long times, the variation of $\tilde{C}(t)$ is controlled by the slowest streamlines: these move first close to the radius $\theta=0$, then along the cell outer boundary ($r \approx R$) and, finally move back to the origin close to the radius $\theta=\pi$ (Fig. 1). Note that the velocity is minimum near the boundary of the cell along the x axis ($r \approx R$ and $\theta \approx 0$ or π), where both v_r and v_θ are small. Let us now estimate the transit time $\tau(\Psi_0)$ along such a slow trajectory. In the initial part ($\theta \approx 0$) we can put $\cos \theta = 1$ in Eq. (11a) and integrate

with respect to r . One obtains the following expression of the time $t(r)$ necessary to reach radius r after starting from the origin at $t=0$:

$$t(r) = 1 \left/ \frac{M}{2\pi dR^3} \left\{ -\frac{r}{R} - \frac{1}{2} \left[\ln\left(\frac{R-r}{r}\right) - \ln\left(\frac{R+r}{r}\right) \right] \right\} \right. \quad (12)$$

When the particle becomes close to the outer boundary ($r \rightarrow R$), Eq. (12) gives

$$R - r \cong 2R \exp \left[-2 \left(1 + \frac{Mt(R)}{2\pi dR^3} \right) \right]. \quad (13)$$

Let us now compute the time necessary to move from angle θ to angle $\pi/2$ on trajectories close to the outer boundary ($R \cong r$) by integrating Eq. (11b) with respect to θ :

$$t(\theta) - \frac{\tau}{2} = \frac{\pi dR^3}{M} \ln \tan \frac{\theta}{2}, \quad (14)$$

where τ is the global time to go from the dipole to the outermost point of a given trajectory and back. Due to the symmetry of the problem one has $t(\pi/2) = \tau/2$ and, in the part of the trajectory where $\theta \rightarrow 0$, Eq. (14) becomes

$$\theta \cong 2 \exp \left[\left(t(\theta) - \frac{\tau}{2} \right) \frac{M}{\pi dR^3} \right]. \quad (15)$$

Equations (13) and (15) are simultaneously valid in the very low velocity region where one has both $\theta \cong 0$ and $r \cong R$: the streamfunction there is obtained by combining Eqs. (11c), (15), and (13) so that

$$\Psi \rightarrow \Psi(\tau) = \frac{4M}{\pi d e^2 R} \exp \left(-\frac{M\tau}{2\pi dR^3} \right). \quad (16)$$

We have used the fact that any point (r, θ) is uniquely characterized by the transit time for the trajectory through it. Here, $\Psi(\tau)$ is a monotonically decreasing function of τ and $\Psi \rightarrow 0$ when $\tau \rightarrow \infty$. After a time τ , only particles following trajectories corresponding to $\Psi < \Psi(\tau)$ (the slowest ones) have not yet returned to the origin. From the definition of the streamfunction one shows classically that $[\Psi(\tau) - \Psi(\infty)]d = \Psi(\tau)d$ is the total flow rate associated with these slow flow lines that still carry the original displaced fluid. Therefore, $\Psi(t)d/Q$ is the mean relative fraction $\tilde{C}(t)$ of this fluid in the outgoing flow so that

$$\tilde{C}(t) = \frac{4a}{\pi e^2 R} \exp \left(-\frac{t}{\tau_c} \right) \quad (17a)$$

with

$$\tau_c = \frac{2\pi dR^3}{Qa}. \quad (17b)$$

Thus, for a finite size model, $\tilde{C}(t)$ decreases as $t^{-1/3}$ at short times and exponentially as e^{-t/τ_c} at long times when the external boundary condition becomes dominant. Since the total volume V_i of the model is $\pi e R^2$, the volume $V(t)$ of initial solution displaced at time t satisfies (Eq. 8)

$$V(t) = \int_0^t Q \tilde{C}(t) dt = \pi d R^2 - \int_t^\infty Q \tilde{C}(t) dt$$

so that, at long times where expression (17a) is valid,

$$V(t) = \pi d R^2 \left[1 - \frac{8}{\pi e^2} \exp \left(-\frac{t}{\tau_c} \right) \right]. \quad (18)$$

C. Exponential decay rate for a finite separation and a finite cell

Let us now assume that the source-sink distance is finite. The complex potential becomes

$$W(z) = \frac{Q}{2\pi d} \left[\ln \left(z - \frac{a}{2} \right) - \ln \left(z + \frac{a}{2} \right) - \ln \left(z - \frac{2R^2}{a} \right) + \ln \left(z + \frac{2R^2}{a} \right) \right]. \quad (19)$$

The corresponding flow lines have been shown in Fig. 1 for $R/a=5$. One cannot compute analytically $\Psi(\tau)$ in the long-time limit but the time constant τ_c can be obtained by taking the approximation of Eq. (11b) in the limit $\theta \cong 0$ and $r \cong R$. In this limit the tangential velocity v_θ becomes

$$v_\theta = R \frac{d\theta}{dt} = \frac{\theta R Q}{2\pi d} \left(\frac{1}{(R-a/2)^2} - \frac{1}{(R+a/2)^2} + \frac{1}{(R+2R^2/a)^2} - \frac{1}{(R-2R^2/a)^2} \right). \quad (20)$$

After rearranging Eq. (20), one obtains

$$\frac{d\theta}{dt} = \theta \frac{QRa}{\pi d} \left(\frac{1+a^2/4R^2}{(R^2-a^2/4)^2} \right) \quad (21)$$

so that the time constant τ_c for the long-time concentration variation given by Eq. (17b) is

$$\tau_c = \frac{2\pi dR^3}{Qa} \frac{(1-a^2/4R^2)^2}{1+a^2/4R^2}. \quad (22)$$

This formula reduces to Eq. (17b) in the limit $a=0$ and predicts a relative decrease of τ_c with respect to the above value of the order of $3a^2/4R^2$.

D. Numerical computations

In the above sections, we have computed the shape of the concentration exit profile in the pure-dipole limit both for an infinite size cell and, at long times, for a finite-size cell. It is possible to extend the calculation to the case of a finite separation between source and sink, provided the cell is infinite.¹⁹ However, the transit time distribution cannot be computed analytically at all times in the fully realistic case when both the source-sink interval and the system size are finite. We present here the results of the numerical computation of this distribution for this case, retaining however the 2-D convective approximation.

First, we compute the transit time $\tau(\theta)$ corresponding to trajectories leaving the source at an angle θ with respect to the (x) axis joining the source and the sink. We simply integrate the two coupled ordinary differential equations

$$\frac{dr}{dt} = \text{grad}[\text{Re } W(z)] \quad (23)$$

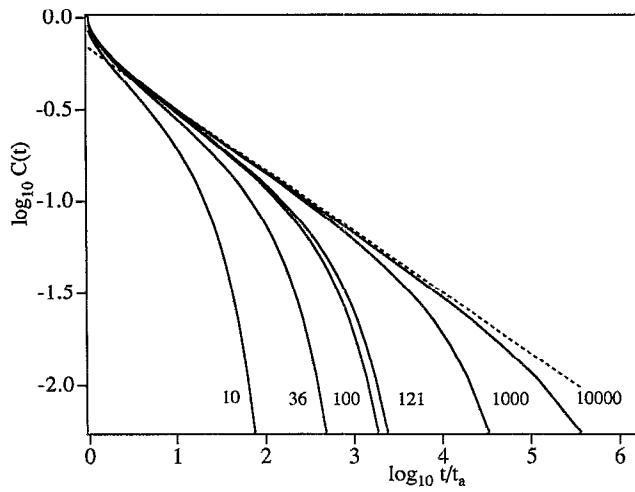


FIG. 3. Variation of $\log_{10} C$ with $\log_{10} t/t_a$ for numerical simulations with a 2-D velocity field and finite R/a values increasing from left to right. $C(t)$ is here the normalized concentration and t_a is the time of first arrival of the injected fluid to the sink point. The value of $(2R/a)^2$ is shown for each curve.

with W , as given in (19), using a variable-step, variable-order backward difference routine.²⁰ $\tau(\theta)$ is computed for 180 equally spaced θ values between 0 and $179\pi/180$. Then the interval $[0, \pi/180]$ is again divided in 100 parts in order to investigate precisely the exponential relaxation at long times. As explained above, the relative concentration $\tilde{C}(t)$ of initial fluid in the outflowing solution at a given time is equal to the fraction of the flow rate for which the transit time is larger than t . Near the source point, the flow is radial and isotropic so that the flow rate is equally distributed between all θ values. Since the slowest flow lines correspond to $\theta = \pi$, and particles are emitted uniformly in θ , one has $\tilde{C}(t) = [\pi - \theta(t)]/\pi$, where $\theta(t)$ is the angle corresponding to the transit time t .

Figure 3 gives a log-log plot of $\tilde{C}(t)$ as a function of the ratio t_{num}/t_a (t_a being the first arrival time), for several values of the ratio R/a . The time scale t_{num} used in the simulations is nondimensional and related to the physical one by

$$t_{\text{num}} = t \frac{2Q}{\pi a^2} \quad (24)$$

It is only at the largest value of R/a ($R/a=50$) that one observes a slope $-1/3$ corresponding to the infinite medium approximation over a significant part of the curve. The minimum slopes on the other curves are significantly lower, particularly for the values $R/a=3$ and $R/a=5.5$ that correspond to the laboratory experiments to be discussed in Sec. III. We also observe that the range of times over which the slope of the log-log curve is approximately constant increases markedly with R/a being practically non-existent at the lowest values. By plotting $\tilde{C}(t)$ in semilogarithmic coordinates, one verifies that the exponential relaxation regime is indeed reached at long times.

In order to obtain a precise value of τ_c , particularly at large values of R/a , it has been necessary to extend the

TABLE I. Variation of the characteristic relaxation times τ_c for the exponential long time part of the concentration variation and of the exponent in the power-law part of the concentration variation at intermediate times. The time scales are those used in the numerical simulations and the physical time values can be obtained by the relation $T_{\text{phys}} = (\pi a^2 d / 2Q) T_{\text{num}}$.

R/a	τ_c [Eq. (17b)]	τ_c [Eq. (22)]	τ_c (numerical)	Exponent
1.58	15.81	11.6	11.7	-0.56
3.0	108	99.4	100.3	-0.44
5.0	500	485.2	484.7	-0.39
5.5	665.5	649.2	648.2	-0.385
15.8	15 811	15 762	15 753	-0.35
50	500 000	499 900	499 000	-0.34

curves at long times by using θ values closer to π as reported above. Table I displays the values of τ_c obtained by the numerical computation, and those determined analytically from Eqs. (17b) and (22), for several values of R/a (after taking into account the nondimensionalization). We see that the agreement between the analytical and numerical computations of the relaxation times is always better than 1% when the finite source-sink distance correction discussed in the previous section is applied. This correction can be as high as 35% for $R/a=1.5$ and 10% for $R/a=3$.

In summary, the numerical computations indicate the very strong influence of finite R/a values, which increase the apparent exponent of the power law variation at intermediate times and reduces its domain of validity. These computations also confirm the exponential cutoff at long times, which is in very good agreement with the analytical calculation.

III. DISPERSION EXPERIMENTS

In order to verify that the above discussion gives a realistic view of the tracer spreading process, we have carried out experiments in circular Hele-Shaw cell geometries. A further motivation is that in future studies of dipole dispersion phenomena, experiment may prove more efficient than calculation in investigating the influence of realistic features such as permeability heterogeneities and complex boundary shapes. We have selected the Hele-Shaw system, in preference to a slab of porous material, for a number of reasons: the geometry is easier to control, the dispersion process is simpler to model numerically (at least at early times), visualization is easier, and permeability variations can be introduced in a controlled manner. In addition, this system provides a good representation of fractures, which are an important component of low-porosity rocks and in waste containment problems.

A. Experimental setup

The model fracture²¹ consists of the space between two circular and parallel 1 cm thick glass plates (Fig. 4). The fracture aperture is fixed by a 1 mm thick rubber ring placed between the plates at their edges. To prevent water leaks, silicon glue and elastic clips uniformly distributed around the cell are used. Two holes of 1 mm diameter have been drilled in the upper glass plate; they are symmetrical

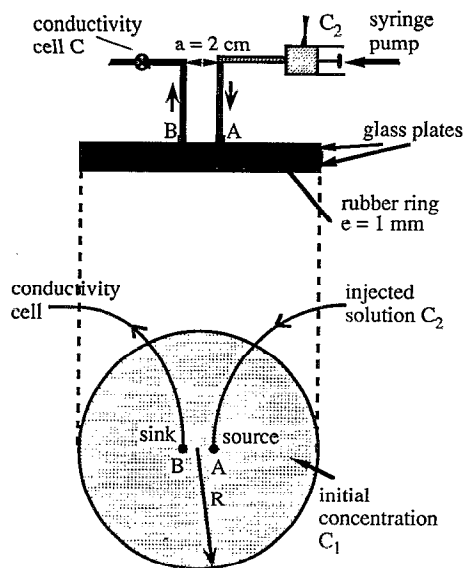


FIG. 4. Schematic view of the experimental setup with the circular cell used in the experiments.

with respect to the plate center and spaced by $a=2$ cm. They are used as the fluid inlet A and outlet B, and represent, respectively, the source and the sink of the dipole. We have used two cells of different radii: $R=6$ cm and $R=11$ cm, but with the same thickness and the same spacing a in order to study the influence of the ratio R/a .

The cell is initially filled with a solution of water and sodium nitrate of salt mass concentration C_1 which flows through the model. Then we inject at point A at the initial time the same solution but with a different concentration C_2 . The total injected fluid volume in all experiments is in the order of 80 ml. The concentration is determined by the electrical conductivity of the fluid. Conductivity variations of the mixture are monitored at the outlet of the cell with a Dionex low volume conductivity detector: The dead volume of the injection and detection circuits are of the order of 0.5 cm^3 compared to respective model volumes of 11.5 and 38 cm^3 . The conductance measurement are performed with a Hewlett Packard 4192A impedance meter at a frequency of 500 kHz for which capacitance effects in the electrodes and measurement circuits are minimized. A thermocouple is inserted near the electrodes in order to correct the conductivity for temperature variations which are recorded simultaneously with those of conductivity. Fluid is injected at a constant flow rate by a Harvard syringe pump with a continuous constant velocity displacement. The flow rates, which vary from 0.006 to 0.15 ml/mn, are controlled precisely and are reproducible to $\pm 1\%$.

In order to measure precisely the distribution of the tracer transit times through the cell, we first determine the dead volume associated with the inlet and outlet tubes by directly connecting both tubes (connection AB). We have analyzed the tracer dispersion in all the tubes (by using the same solutions as in the experiments). The time variation of tracer concentration is Gaussian as expected for Taylor dispersion in a tube and can be fitted to solutions of the

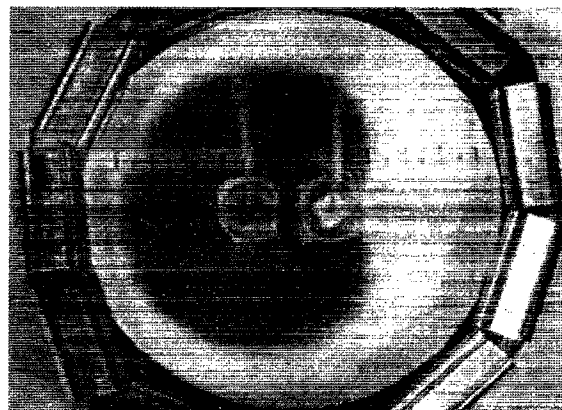


FIG. 5. View of the experimental cell ($R=6$ cm, $a=2$ cm, $d=0.1$ cm) after injection of dye ($Q=0.053$ ml/s, $t=700$ s).

usual convection–diffusion equation. We obtain in this way the mean transit time associated with the dead volume of the connection tubes. These measurements were performed at the beginning of the dispersion experiments in the cell of smallest diameter ($R=6$ cm). Once the experiment has been completed, we rinse the cell by injecting the solution of concentration C_1 at point B until it is again saturated with that solution (during the cleaning process, we inject about five times the solution volume used during the experiment itself).

B. Experimental measurements

We first examine visually the spreading of an injected solution containing some dye (amaranth red) in Fig. 5. At very short times, the dyed part of the surface has a circular shape because of the radial velocity field very close to the source. As expected, the first tracer particles reaching the sink point follow the direct path from the source. At later times, the dyed surface has the shape of a cardioid and is quite similar to that shown in Fig. 2 (continuous lines) corresponding to the 2-D approximation. Compared to the approximation of the perfect dipole in an infinite 2-D medium (dotted lines), the shape of the invaded zone is very similar at short times; at longer times the growth is constrained as expected by the cell boundary (particularly in the direction of the source-sink axis) and a dye-free zone is seen near the rim. The growth of the cardioid slows with time since the velocity of the dye particles located at the boundary quickly decreases with distance.

Next we measured the time variation $C(t)$ of the conductivity of the fluid flowing out of the model for different flow-rate values. Figure 6 displays the variation of the logarithm of the normalized concentration $\bar{C}(t) = [C_2 - C(t)] / (C_2 - C_1)$ as a function of $\log_{10}(t)$ for the two experimental models corresponding to $R/a=5.5$ and $R/a=3$. We note that the asymptotic conductivity C_2 is measured directly at the outlet syringe, since small errors in the value of C_2 may induce large changes of the slope $\delta \ln[C(t)] / \delta \ln t$. Both curves have a linear part corresponding to the power-law regime. As expected, the slope

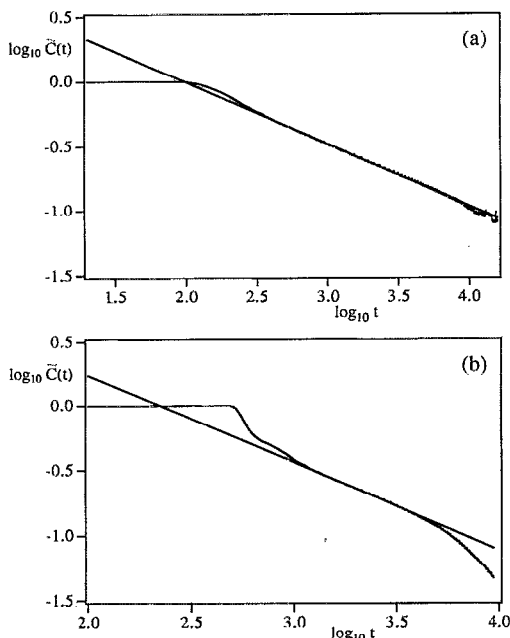


FIG. 6. Variation of $\log_{10} C(t)$ with $\log_{10} t$ ($Q=0.006$ m³/s) for two experimental models: (a) $R/a=5.5$ ($R=11$ cm, $a=2$ cm, $d=0.1$ cm); (b) $R/a=3$ ($R=6$ cm, $a=2$ cm, $d=0.1$ cm).

is larger for the model with the smallest R/a value. This confirms the strong influence of the outer boundary condition; the two slopes are, respectively, equal to -0.48 and -0.6 which is slightly larger than the values from Table I and, as expected, markedly different from the value $-1/3$ for an infinite model. More generally, the values of the exponent depend on the flow rate and range between 0.35 and 0.45 for $R/a=5.5$ while they are of the order of 0.5 for $R/a=3$.

The curve for $R/a=3$ displays a marked downward curvature at long times, corresponding to the transitions toward an exponential relaxation regime. The total injected volume was, however, not sufficient to allow for a direct determination of the characteristic time constant. As expected, this effect was less apparent for $R/a=5.5$ where the relaxation time is about six times larger.

Figure 7 displays the variation of $\bar{C}(t)$ for $R/a=3$ at several flow rate values, as a function of the ratio V_{inj}/V_t of the injected fluid volume and of the fracture volume. The variation is compared to the corresponding theoretical curve of Fig. 3 (dotted line). The various experimental curves overlay rather well and their shape follows closely that of the theoretical curves. The shift between these series of data may be due to dead volume effects or errors in the initial time values.

In order to compare more precisely the experimental and numerical results, we have superimposed in Fig. 8 experimental normalized displaced volume variations $V(t)/V_t$ corresponding to different flow rates ($R=6$ cm). Using Eq. (8), $V(t)$ is computed and plotted as a function of the normalized injected volume. We observe first that, as for $\bar{C}(t)$, the variation of $V(t)/V_t$ with V_{inj}/V_t is almost

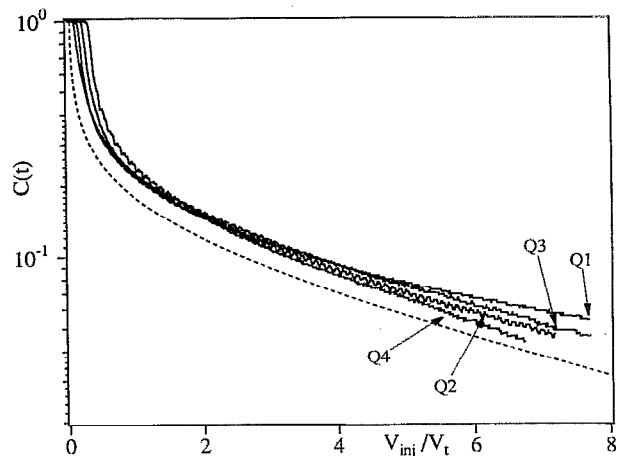


FIG. 7. Variation of the experimental normalized concentration $C(t)$ as a function of the normalized injected volume V_{inj}/V_t for 4 different injection flow rates ($R=6$ cm, $a=2$ cm, $d=0.1$ cm, V_t is the total volume of the experimental cell). The dotted line corresponds to the theoretical predictions of the 2-D convective model with the same values of R and a .

independent of the flow rate (but for the slowest one for which the corresponding curve is slightly above the others). We have also plotted on the same graph variations of $V(t)$ predicted for a perfect dipole in an infinite medium [$2/3$ power law of Eq. (7b)] and curves corresponding to the numerical 2-D computations of the previous section for the same R/a ratio. The latter correspond well to the experimental curves but for a shift in the time scales. On the contrary, the perfect dipole model does not agree with the experimental data at all: this was to be expected since the corresponding variation of $V(t)$ diverges at long times while all experimental variations should tend toward a finite limit.

In summary, all experimental results confirm that the convective 2-D models give a good quantitative description of the dispersion curves except at very low flow rates where

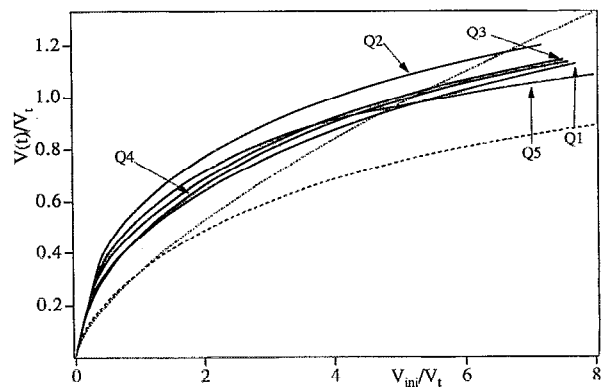


FIG. 8. Variation of the normalized volume $V(t)/V_t$ occupied by the injected fluid as a function of the normalized injected volume V_{inj}/V_t for 4 different injection flow rates ($R=6$ cm, $a=2$ cm, $d=0.1$ cm, V_t is the total volume of the experimental cell). The lower dotted line corresponds to the theoretical predictions of the 2-D convective model with the same values of R and a , the upper dotted line corresponds to the predictions for $a=0$ and $R \rightarrow \infty$.

the displacement of the original solution seems to be slightly accelerated. Therefore, Taylor dispersion due to the Poiseuille flow profile between the plates does not seem to play a dominant role. However, experimental limitations have prevented us from verifying some of the predictions of the convective model, such as the existence of an exponential relaxation process at long times and the corresponding relaxation rate.

IV. NUMERICAL MODELING OF THE EFFECT OF TAYLOR DISPERSION AND MOLECULAR DIFFUSION ON THE DISPERSION PROCESS

In order to investigate the limits of validity of the convective model, we now turn to a more realistic numerical study. We perform Monte-Carlo numerical simulations, taking into account both the effect of the Poiseuille velocity profile between the parallel plates and molecular diffusion.²² This will allow us to analyze the effects of the Taylor dispersion process and of the diffusive exchange of the tracer in very low velocity zones.

In these simulations, the tracer is assumed sufficiently dilute that tracer particles move independently of each other. One follows the radial and vertical displacements of a large number of particles moving in the Hele-Shaw cell. The initial condition consists of releasing all the particles at $t=0$ from a given small initial radius $r_0=1$ mm at a height z_0 chosen in an interval of thickness d . The starting positions of the particles on the circle are uniformly distributed according to the radial nature of the flow field close to the source. In order to reproduce the experimental conditions, z_0 is modulated according to the local flux of fluid with a parabolic profile. The motion of each particle is the combination of the effects of molecular diffusion (represented by a Brownian motion) and convection.

We use the Hele-Shaw approximation in which the local velocity is taken to be the product of the 2-D dipole field computed from Eq. (19) and the parabolic Poiseuille velocity profile between the plates. The Hele-Shaw approximation is valid except very near the injection point and the rim of the plates, because of the large ratio between the spacing of the plates and their radius. The duration Δt of each step is selected to decrease inversely with the local velocity in order to keep the length of the convective displacements below a limit. The random Brownian motion is simulated by performing at each time step a random jump of length $\sqrt{6D_m\Delta t}$, where D_m is the molecular diffusion coefficient and Δt is the time step; the direction of the steps is random and distributed uniformly in all directions. The amplitude $\sqrt{6D_m\Delta t}$ of the random steps has been chosen so that the variance of any coordinate after n independent steps is

$$[x(t) - x(0)]^2 = n6D_m\Delta t \frac{1}{3} = 2D_mt, \quad (25)$$

where the factor $1/3$ represents the variance of a random coordinate chosen uniformly on a unit sphere.

Zero flux boundary conditions at the top, bottom, and rim of the cell are implemented by suppressing those random steps that would take the particle outside the cell. The

sequence of convective and diffusive displacements is repeated until the particle arrives within a distance r_0 from the outlet: the corresponding time, $n\Delta t$, is the transit time of the particle. The process is repeated for a very large number of particles (up to 30 000). The total computing time is typically several hours on a Sun Sparc or a Silicon Graphics Indigo workstation. After all the individual transit times have been determined, one computes the equivalent of the experimental concentration variation curves: it is the complement of the integrated histogram of the individual transit times. In order to take into account the very broad transit time distribution and the lower number of particles at very long times, three different spacings between histogram points were used.

Figures 9(a)–9(d) display the simulated concentration variation curve obtained for the several values of flow rate, for the two outside diameters of 6 cm [(a) and (b)] and 11 cm [(c) and (d)], and for the thickness $d=0.1$ cm. Both log-log plots and semilog plots are shown to allow the separate identification of the power law and the exponential relaxation. The flow rates are characterized by a Péclet number $Pe=Q/D_md$ (this definition has been chosen because it is independent of position in the cell). All times have been normalized by that of first arrival in the purely convective 2-D case at the same flow rate: the convective curve has also been superimposed onto the others. At all velocities but the smallest, the variation of $C(t)$ with the normalized time is almost independent of the flow rate in the range of t for which $C(t)$ follows a power law [Figs. 9(a) and 9(c)]. At times short compared to the transverse diffusion time, the Taylor approximation is not valid and the first arrival time is shorter than in the 2-D approximation (it corresponds to the maximum of the velocity profile in the center of the channel, equal to 1.5 times the mean velocity). At very long times, in the exponential decay regime, the variations of $C(t)$ at the fastest flow rates coincide with the convective 2-D model [Figs. 9(b) and 9(d)].

At lower velocities, the decay of the concentration toward its asymptotic value is accelerated. This can be explained by diffusion of tracer located close to the rim of the model toward higher velocity flow lines. The curves from Figs. 9(b) and 9(d) seem to indicate that at long times there is a transition toward an exponential relaxation with a time constant τ_{c2} equal to a fraction of τ_c which seems to be roughly constant. Changing the flow rate only modifies the fraction of tracer particles for which the transit time is shortened by this effect.

Let us now estimate the fraction of the total flow rate influenced by molecular diffusion in the part of the fluid particle trajectories located near the edge to the rim ($r \approx R$). Using Eqs. (14) and (17b), we estimate that the transit time in this region is of the order of τ_c : this allows the tracer to diffuse over a distance $\delta r \approx \sqrt{D_m\tau_c}$ from the model rim ($r=R$). The streamfunction varies then from 0 to $\delta\Psi \approx v_\theta(r)\delta r$ so that

$$\delta\Psi \approx \frac{Qa}{dR^2} \sqrt{D_m\tau_c} \approx \sqrt{\frac{QaD_m}{dR}}. \quad (26)$$

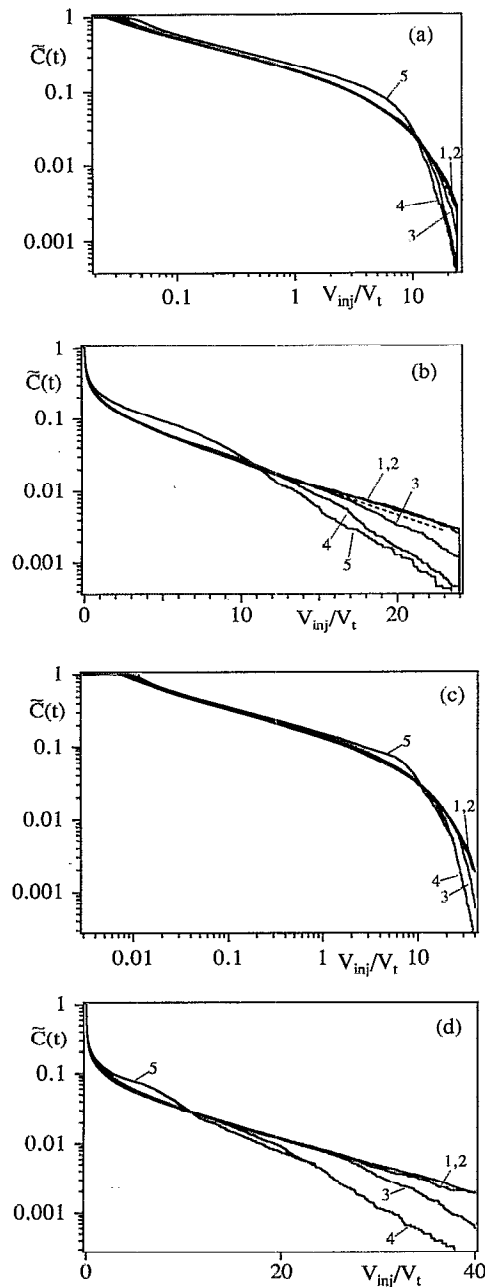


FIG. 9. Numerical Monte-Carlo simulation results compared to 2-D convection computation. Variation of normalized concentration $\bar{C}(t)$ computed using Monte-Carlo simulations as a function of the normalized injected volume V_{inj}/V_t for different injection flow rates. (5— $Pe=Q/D_m d=142$, 4— $Pe=1420$, 3— $Pe=7100$, 2— $Pe=142\,000$, 1— $Pe=710\,000$). The dotted line (coinciding most of the time with curves 1 and 2) corresponds to the 2-D convective simulation. (a) log-log plot; (b) semilog plot; ($R=6$ cm, $a=2$ cm, $d=0.1$ cm); (c) log-log plot; (d) semilog plot; ($R=11$ cm, $a=2$ cm, $d=0.1$ cm).

The perturbed flow lines correspond to Ψ values between 0 and $\delta\Psi$: they represent a relative fraction $\delta Q/Q = \delta\Psi d/Q$ of the total flow so that

$$\frac{\delta Q}{Q} \approx \sqrt{\frac{1}{Pe}} \sqrt{\frac{a}{R}} \quad (27)$$

Here, $\delta Q/Q$ is the order of magnitude of the relative concentration value \bar{C} below which the relaxation curve will be perturbed: for $Pe \approx 7100$, corresponding to curve 3, one has: $\delta Q/Q \approx 7 \cdot 10^{-3}$ ($R/a=3$) in reasonable order of magnitude agreement with the numerical simulation curves of Figs. 9(a)–9(d). We also verify qualitatively that the effect of diffusion decreases with the flow rate and is negligible for the two highest Pe values [in this case, $\bar{C}(t)$ coincides very well with the 2-D convective variation]. Equation (27) also predicts that the perturbation should slowly decrease at larger values of the radius R for a given Pe value: this is indeed the case in Fig. 9 for $Pe=7100$. Let us note that the term $1/\sqrt{Pe}$ is reminiscent of boundary layers effect which involve transverse molecular diffusion as in the present case. At the lowest velocity which we analyzed ($Pe=142$), the power law part of the curve is significantly higher than the convective curve: it is likely that diffusion is strong enough so that at intermediate times tracer can diffuse into low velocity outer zones and move out only later.

V. CONCLUSIONS

We have shown in the present paper that transmission tracer dispersion in a dipole geometry has characteristics completely different from those of “normal” Gaussian tracer dispersion in 1-D flows in homogeneous porous media.

Once the global size R of the system is large compared to the source-sink distance a , the tracer concentration variation follows a power law in time when the penetration depth of the corresponding particle trajectories is in the range between a and R . The limit of the exponent is $-1/3$ when $R/a \rightarrow \infty$; at lower R/a , its value becomes nearer 0.5. At very long times, a cutoff appears and the tracer concentration decays exponentially with a time constant depending on the global size of the system. This exponential relaxation may be accelerated by molecular diffusion into and out of low velocity zones close to the boundary. This effect is important at low flow rates and at large R/a . Other than these effects, the convective 2-D model neglecting the parabolic velocity profile between the plates and molecular diffusion accounts for most experimental observations at medium and long times. Only at very low flow rates is molecular diffusion significant. At very short times, the dispersion is controlled by short flow paths between the source and the sink. The transit time distribution is then also influenced by the diffusion across the liquid layer: this determines the effectiveness of the Taylor dispersion.

In conclusion, the results reported in this paper demonstrate that, in a layered or fracture geometry, the drainage of an initially saturating fluid by a dipole flow is very inefficient because of the rapid increase of the transit time with distance. These results might be extended to a thin layer of porous medium by replacing molecular diffusion by the (more significant) convective dispersion associated with porous media flows. A further valuable extension of our results would involve a systematic study of the char-

acteristics of the long-time tail, since field configurations involve enormous values of R/a .

ACKNOWLEDGMENTS

This work has been conducted under the auspices of a NATO Collaborative Research Grant between the City College of New York and ESPCI. I.I. and J.P.H. wish to thank the Département de Physique de l'École Normale Supérieure for the use of their computing facilities.

¹J. Bear, *Dynamics of Fluids in Porous Media* (Elsevier, New York, 1972).

²F. A. L. Dullien, *Porous Media, Fluid Transport and Pore Structure* (Academic, New York, 1979).

³J. A. Barker and J. H. Black, "Slug tests in fissured aquifers," *Water Resour. Res.* **19**, 1556 (1983).

⁴J. J. Fried, *Groundwater Pollution* (Elsevier, Amsterdam, 1975).

⁵J. J. Fried and M. A. Combarous, "Dispersion in porous media," *Adv. Hydrosci.* **7**, 169 (1971).

⁶E. Guyon, J. P. Nadal, and Y. Pomeau (editors), *Disorder and Mixing* (Kluwer, Dordrecht, 1989).

⁷L. W. Lake and H. B. Carroll (editors), *Reservoir Characterization* (Academic, New York, 1986); J. R. L. Allen, *Sedimentary Structures* (Elsevier, Amsterdam, 1974).

⁸K. H. Coats and B. D. Smith, "Dead-end pore volume and dispersion in porous media," *Trans. AIME* **231**, 73 (1964).

⁹C. H. Ward, W. Giger, and P. L. McCarty, *Ground Water Quality* (Wiley, New York, 1985).

¹⁰J. P. Hulin and D. Salin, "Experimental studies of dispersion in model and natural porous media," in Ref. 6.

¹¹Of course, various approximations for higher dimensional dispersion have been considered; see, for example, W. E. Brigham, "Mixing equations in various geometries," *SPE Res. Eng.* **1**, 203 (1986); L. W.

Gelhar and M. A. Collins, "General analysis of longitudinal dispersion in nonuniform flow," *Water Resour. Res.* **7**, 1511 (1971); R. Smith, "The early stages of contaminant dispersion in shear flow," *J. Fluid Mech.* **111**, 107 (1980).

¹²E. B. Buffham and M. A. Naumann, *Mixing in Continuous Flow Systems* (Wiley, New York, 1983).

¹³J. Koplik, S. Redner, and D. Wilkinson, "Transport and dispersion in random networks with percolation disorder," *Phys. Rev. A* **37**, 2619 (1988).

¹⁴J. A. Hoopes and D. R. F. Harleman, "Wastewater recharge and dispersion in porous media," *J. Hydraul. Div. ASCE* **93**, 51 (1967).

¹⁵D. B. Grove and W. A. Beetem, "Porosity and dispersion constant calculations for a fractured carbonate aquifer using the two-well tracer method," *Water Resour. Res.* **7**, 128 (1971).

¹⁶P. S. Huyakorn, P. F. Andersen, O. Güven, and F. J. Molz, "A curvilinear finite element model for simulating two-well tracer tests and transport in stratified aquifers," *Water Resour. Res.* **22**, 663 (1986).

¹⁷A. C. Gringarten *et al.*, "Modélisation du fonctionnement d'un doublet hydrothermique sur le site du Bonnaud," *Rap. 79 SGN 063 GTH*; "Stockage longue durée en mappe phréatique de calories à basse température pour l'habitat," *Rap. 79 SGN 326 GTH*, Bur. Rech. Geol. Min., Orleans, France (1979).

¹⁸G. I. Taylor, "Dispersion of soluble matter in solvent flowing slowly through a tube," *Proc. R. Soc. London Ser. A* **219**, 186 (1953); R. Aris, "On the dispersion of a solute in a fluid flowing through a tube," *ibid.* **235**, 67 (1956).

¹⁹J. Koplik and S. Redner (unpublished).

²⁰NAG Fortran Library (Numerical Algorithms Group Ltd., Oxford, 1993).

²¹I. Ippolito, "Etude de phénomènes de transport et de dispersion de traceurs dans des milieux fracturés," Thèse de Doctorat, Université Pierre et Marie Curie, Paris, 1993.

²²A Monte Carlo method is applied to a somewhat similar convective dispersion problem in C. J. van der Hoek, "Contamination of a well in a uniform background flow," *Stoch. Hydrol. Hydraul.* **6**, 191 (1992).